Spin-orbit coupling for photons and polaritons in microstructures

V. G. Sala[1,2], D. D. Solnyshkov[3], I. Carusotto[4], T. Jacqmin[1], A. Lemaître[1], H. Terças[3], A. Nalitov[3], M. Abbarchi[1,5], E. Galopin[1], I. Sagnes[1], J. Bloch[1], G. Malpuech[3], A. Amo[1]

[1]*L aboratoire de Photonique et Nanostructures, LPN/CNRS, Route de Nozay, 91460 Marcoussis, France*

[2]*Laboratoire Kastler Brossel, Université Pierre et Marie Curie, École Normale Supérieure et CNRS, UPMC Case 74, 4 place Jussieu, 75252 Paris Cedex 05, France*

[3]*Institut Pascal, PHOTON-N2, Clermont Université, University Blaise Pascal, CNRS, 24 avenue des Landais, 63177 Aubière Cedex, France*

[4]*INO-CNR BEC Center and Dipartimento di Fisica, Università di Trento, I-38123, Povo, Italy*

[5]*Laboratoire Pierre Aigrain, École Normale Supérieure, CNRS (UMR 8551), Université Pierre et Marie Curie, Université D. Diderot, 75231 Paris Cedex 05, France*

Supplemental Material

A Higher energy states of the hexagonal molecule

The polariton benzene molecule employed in our studies is made out of six overlapping cylindrical micropillars. In a single micropillar the three-dimensional confinement of polaritons results in discrete energy levels whose spacing is determined by the diameter of the molecule and the exciton-photon detuning. In our structure, their diameter is 3 μm and the photon-exciton detuning -5 meV, giving rise to a splitting between the lowest and first excited states on the order of 2 meV [1]. The spatial overlap of the micropillars creates a coupling between the ground states of adjacent pillars of 0.3 meV, resulting in the molecular energy levels $E(n)$, $n = 0,1,2,3$. They can be studied in energy-resolved photoluminescence experiments at low power, as shown in Fig. 1 and in Fig. S1(a). For energies above 1567 meV, we observe the emission from the molecular eigenstates arising from the coupling between the first excited states of the pillars. In Fig. S1(b)-(c) we show the measured spatial pattern corresponding to the lowest two, labeled $E(4)$ and $E(5)$.

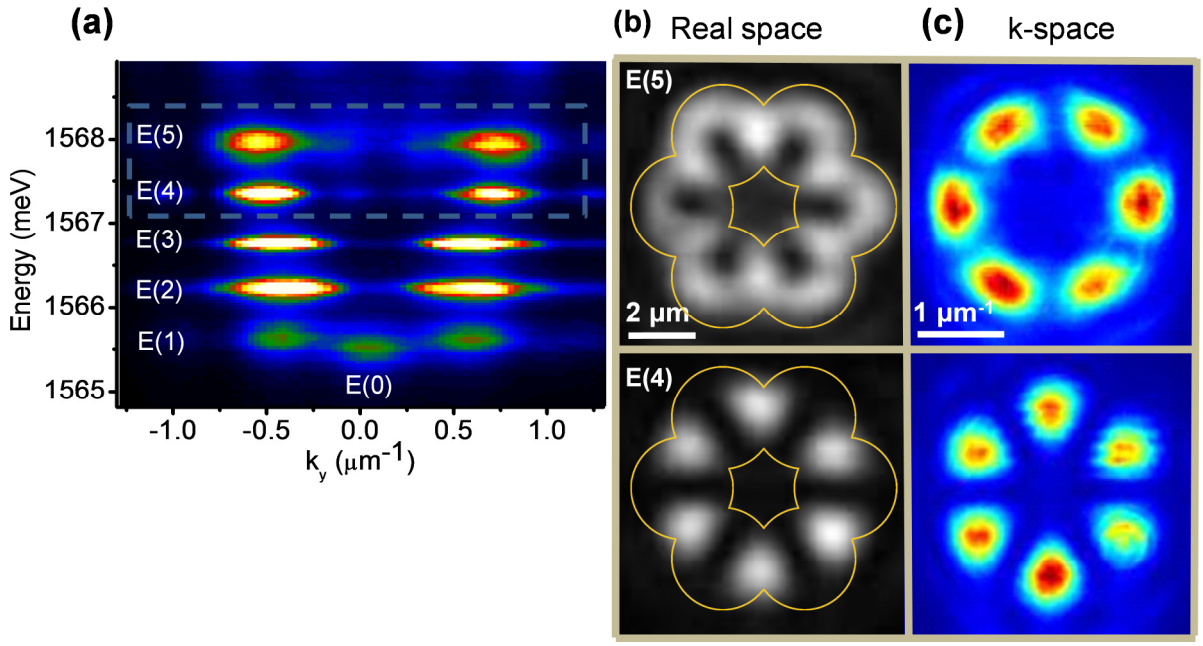

Figure S1. (a) Photoluminescence spectrum in the conditions of Fig. 1(b) of the main text with extended energy range, allowing the observation of higher energy states. In particular, $E(4)$ and $E(5)$ are the lowest two molecular eigenstates arising from the coupling of the first excited states of the individual micropillars. (b) Real- and (c) momentum-space emission from states $E(4)$ and $E(5)$.

B Tunnel coupling and next-nearest neighbor effects

The value of tunnel coupling of 0.3 meV for the lowest energy states was measured in two coupled micropillars with the same diameter and overlap as the micropillars designed in the hexagonal molecule [2]. In addition to nearest-neighbor coupling, next-nearest-neighbour coupling is also possible, and it has been evidenced in the polariton honeycomb lattice described in Ref. [3]. This honeycomb lattice was made out of overlapping micropillars of the same diameter and center-to-center distance than those of the hexagonal structure considered here. The polariton dispersion in the lattice was well fitted using a tight binding

model with nearest-neighbor coupling of 0.25 meV and next-nearest-neighbor coupling of -0.02 meV.

In the actual hexagonal molecule, next-nearest-neighbor tunneling alters the energy splittings between the different $E(n)$ levels. Nevertheless, next-nearest-neighbor coupling does not seem to play a major role in spin-orbit effects. This is probably due to its reduced value compared to the nearest-neighbor coupling. Its negligible influence is confirmed by the good quantitative agreement between the polarisation textures reported in Figs. 4 and 5 of the main text and those expected from the tight-binding model without next-nearest-neighbor coupling (Fig. 2).

C Visibility of fringes for states $E(1)$ and $E(2)$ in Fig. 1

Disregarding the spin degree of freedom, eigenstates corresponding to $E(1)$ and $E(2)$ levels are doubly degenerate. These levels contain eigenstates with angular momenta $l = \pm 1$ and $l = \pm 2$, respectively. For each one of them the emission in the low power regime arises from a linear combination of states with opposite orbital momentum l. For instance, in the case of the $E(1)$ level, the emission arises from the combination of $l = +1$ and -1 eigenstates:

$$|\psi_1(j,\theta)\rangle = \sum_j 12^{-1/2}\, e^{+i2\pi j/6}|j\rangle + 12^{-1/2}\, e^{-i2\pi j/6+i\theta}|j\rangle, \quad \text{(A)}$$

where we have assumed that both states have equal probability of being populated. $|j\rangle$ is the lowest energy state of each individual micropillar and θ is a relative phase whose value, in the spontaneous emission regime, changes randomly in time. When doing an interferometric experiment integrated in time as the one shown in Fig. 1, in which the emission from a reference pillar interferes with that of the whole molecule, this random phase has an important influence in the visibility of fringes.

As explained in the main text, maximum visibility takes place only at the positions of the micropillar used as a reference [arrow in Fig. S2(c)] and of that located opposite to it [dashed arrow in Fig. S2(c)]. Both of these pillars share instantaneously the same phase structure with an overall change of π, independent of the relative random phase θ. This results in a high fringe visibility. Intermediate pillars mix different phases from the $l = \pm 1$ states. In those pillars, the interference with the reference pillar results in a pattern that changes in time depending on the relative random phase between the two substates. When averaging in time as done in our experiment, the fringe visibility reduces to zero at points of the molecule located $\pm 90°$ from the reference pillar. This is shown in Fig. S2(k), where we plot the measured visibility of fringes at each point in space for the emission corresponding to level $E(1)$. The visibility was obtained from the amplitude of the real part of the off-diagonal Fourier transform analysis performed on the interferometric images.

We can qualitative reproduce this behavior by calculating the expected fringe visibility for the state described by Eq. (A) when interfering with the emission from the reference pillar. This can be done by computing the absolute value of the following quantity:

$$V(\varphi) = \frac{1}{2\pi}\int_0^{2\pi} \frac{\psi_1(0,\theta)\psi_1^*(\varphi,\theta)}{|\psi_1(0,\theta)||\psi_1^*(\varphi,\theta)|}\, d\theta$$

where we have parameterized $i2\pi j/6$ in Eq. (A) as φ. In this case of $l = \pm 1$, φ corresponds to the geometric angle when turning around the molecule [see sketch in Fig. S2(c)]. The calculated visibility of fringes $|V(\varphi)|$ as a function of the geometric angle from the reference pillar is shown in Fig. S2(n). Two points of zero visibility are expected at $\varphi = 90°$ and $270°$, as observed experimentally. The same situation is found for the emission at the energy of $E(2)$, in this case with four points of zero visibility located at $\varphi = 45°, 135°, 225°, 315°$ [Fig. S2(j): experiment; Fig. S2(m): theory].

The $E(0)$ level is non-degenerate and its visibility is high over all the pillars [Fig. S2(l)]. The same situation is expected for $E(3)$. However, in this case, there is a phase jump of π from pillar to pillar, and the wavefunction has a node in between the pillars. This results in no emission at those points and thus, a vanishing visibility in between the micropillars [Fig. S2(i)].

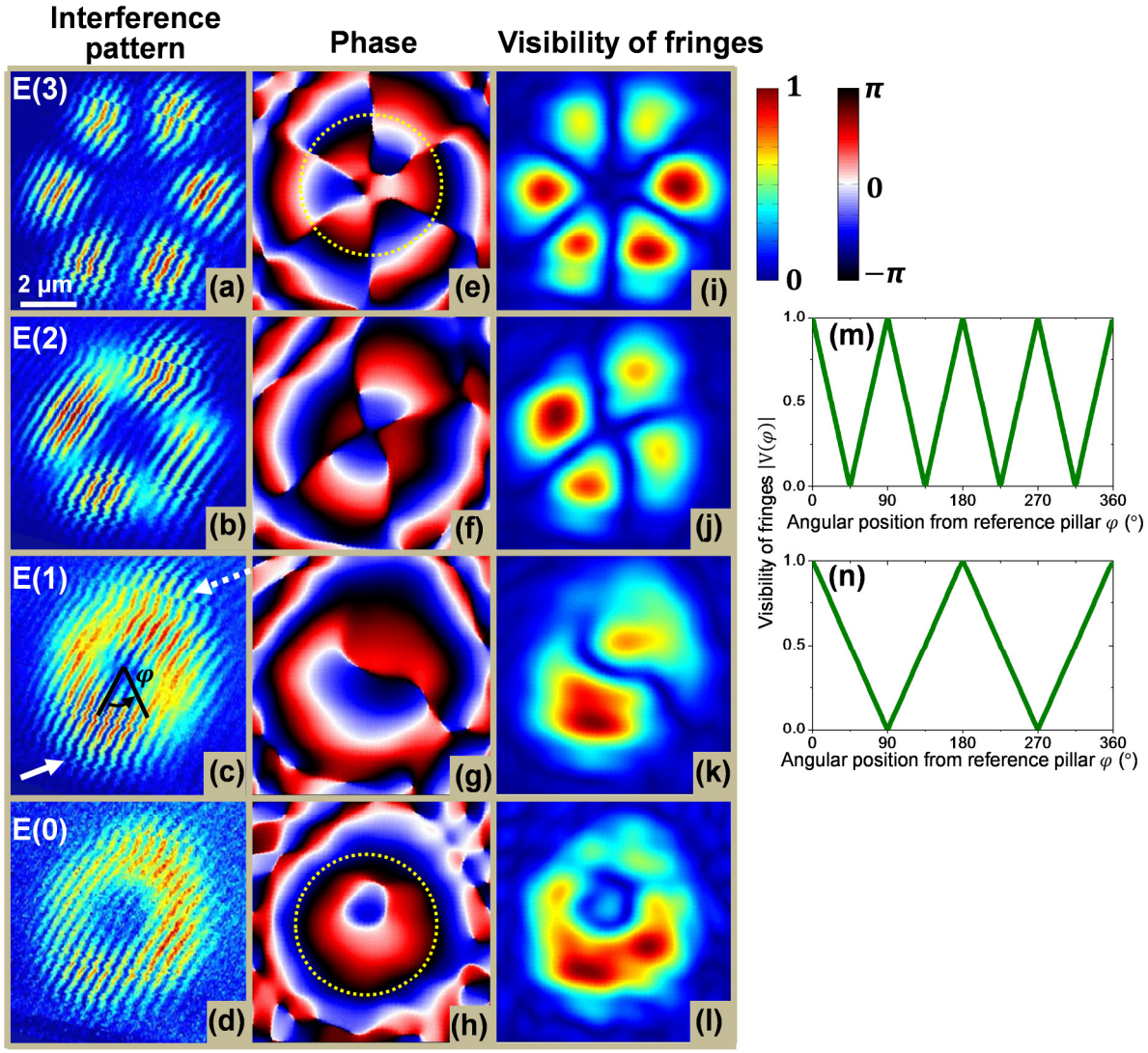

Figure S2. Interference (a)-(d), extracted phase (e)-(h) and visibility of fringes (i)-(l) of the $n = 0,1,2,3$ levels measured in the spontaneous emission regime at low excitation density (conditions of Fig. 1 of the main text). (n-m) Expected visibility of fringes corresponding to the $n = 1$ (n) and $n = 2$ (m) levels.

D Measurement of the polarization structure of the $n = 1$ and $n = 2$ condensed states

The polarization of light emitted at a particular point of the sample can be described in the paraxial approximation as in Born and Wolf [4]. We can define an arbitrary polarization state in the following way:

$$E_x = a_1(\boldsymbol{r})cos\big(\omega\tau + \delta_1(\boldsymbol{r})\big),$$

$$E_y = a_2(\boldsymbol{r})cos\big(\omega\tau + \delta_2(\boldsymbol{r})\big),$$

where $a_{1,2}(\boldsymbol{r})$ describes the amplitude of the electric field along the $\boldsymbol{x}$ and $\boldsymbol{y}$ directions in the plane of the molecule at a given point $\boldsymbol{r}$, ω is the frequency of light and $\delta_{1,2}(\boldsymbol{r})$ are fixed phases for each component. The polarization state is fully determined by the ratio $a_1(\boldsymbol{r})/a_2(\boldsymbol{r})$ and by the phase difference $\delta_2(\boldsymbol{r}) - \delta_1(\boldsymbol{r})$.

The condition for linear polarization is $\delta = \delta_2(\boldsymbol{r}) - \delta_1(\boldsymbol{r}) = m\pi$, with $m = 0, \pm1, \pm2, \ldots$, with the ratio $a_1(\boldsymbol{r})/a_2(\boldsymbol{r})$ defining the direction of polarisation. Circular polarization is obtained under the condition $a_1(\boldsymbol{r}) = a_2(\boldsymbol{r})$, $\delta = \delta_2(\boldsymbol{r}) - \delta_1(\boldsymbol{r}) = m\pi/2$, with $m = \pm1, \pm3, \pm5, \ldots$ Other values of $a_1(\boldsymbol{r})/a_2(\boldsymbol{r})$ and δ result in elliptical polarisations.

A basis of interest is that of circular polarization:

$$\boldsymbol{E}_{\sigma+} = a_{\sigma+}(\boldsymbol{r})cos\big(\omega\tau + \delta_{\sigma+}(\boldsymbol{r})\big)\boldsymbol{x} - i\, a_{\sigma+}(\boldsymbol{r})cos\big(\omega\tau + \delta_{\sigma+}(\boldsymbol{r})\big)\boldsymbol{y},$$

$$\boldsymbol{E}_{\sigma-} = a_{\sigma-}(\boldsymbol{r})cos\big(\omega\tau + \delta_{\sigma-}(\boldsymbol{r})\big)\boldsymbol{x} + i\, a_{\sigma-}(\boldsymbol{r})cos\big(\omega\tau + \delta_{\sigma-}(\boldsymbol{r})\big)\boldsymbol{y},$$

In this basis, a linear polarized state corresponds to $a_{\sigma+}(\boldsymbol{r}) = a_{\sigma-}(\boldsymbol{r})$; the phase difference $\delta_\sigma(\boldsymbol{r}) = \delta_{\sigma+}(\boldsymbol{r}) - \delta_{\sigma-}(\boldsymbol{r})$ sets the direction of the linear polarisation: $\theta = -(\delta_{\sigma+}(\boldsymbol{r}) - \delta_{\sigma-}(\boldsymbol{r}))/2$, with θ the clockwise angle from the $\boldsymbol{x}$ direction.

Experimentally, the polarization state of the emission can be fully described by the Stokes coefficients:

$$S_0 = I_{tot}$$

$$S_1 = \frac{I_x - I_y}{S_0}$$

$$S_2 = \frac{I_{+45} - I_{-45}}{S_0}$$

$$S_3 = \frac{I_{\sigma+} - I_{\sigma-}}{S_0}$$

where $I_{x,y,+45,-45,\sigma+,\sigma-}$ are the emitted intensities when detecting the linearly polarized emission along the x, y axis, the +45º, -45º directions with respect to the x axis, and the $\sigma+, \sigma-$ circularly polarization, respectively. S_1, S_2, S_3, are defined such that they correspond to the degree of polarisation along the same axes. The relation to the $a_{\sigma+}/a_{\sigma-}$ ratio and θ is:

$$\frac{a_{\sigma+}}{a_{\sigma-}} = \frac{S_3 + 1}{S_3 - 1}$$

$$\theta = \frac{1}{2}\arctan\left(\frac{S_2}{S_1}\right)$$

Graphically, the polarization state corresponds to a point in the Poincaré sphere determined by the S_1, S_2, S_3 axis:

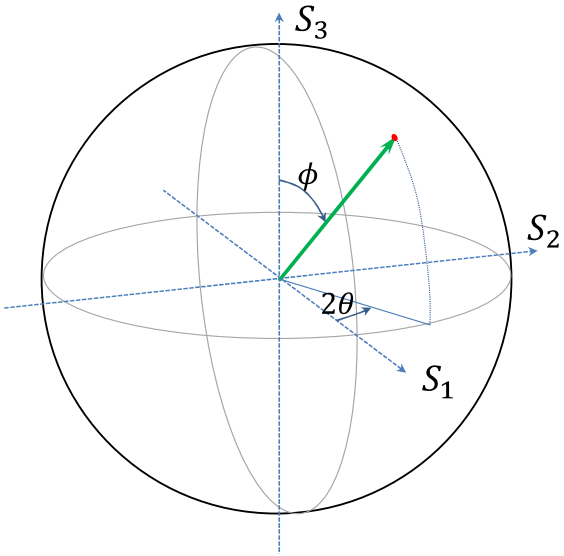

Figure S3. Poincaré sphere representing the polarisation state of the emitted light. Note that $\phi = \arccos S_3$.

In order to reconstruct the linear polarization patterns shown in Figs. 4g and 5g, we measure the Stokes coefficients S_1 and S_2 by using a linear polariser in combination with a half-waveplate. Due to constraints in the experimental set-up, in order to reconstruct the linear polarization map shown in Figs. 4g and 5g we measure S_1 and S_2 along the polarisation axes oriented 22.5º/112.5º and 67.5º/157.5º with respect to the x direction (horizontal) in Figs. 4 and 5. We can redefine the coefficients S_1 and S_2 along those axes:

$$S_1' = \frac{I_{22.5} - I_{112.5}}{S_0}$$

$$S_2' = \frac{I_{67.5} - I_{-157.5}}{S_0}$$

S_3 is measured by using a quarter-waveplate and a linear polarizer.

Figures S4 and S5 show the polarization emission filtered in the different projections needed to reconstruct S_1', S_2', and S_3 corresponding to the situations described in Figs. 4 and 5 of the main text, respectively. The angle α shows the orientation of the polarizers used to analyse the emission with respect to the horizontal axis of the molecule, as defined in the inset. From images (a) through (d) in Figs. S4 and S5 we can extract the direction of the linear polarization of the emission plotted in Figs. 4g and 5g. The angle θ setting the direction of linear polarization at each point in the plane of the figures is calculated from the following expression: $\tan[2 \cdot (\theta + 22.5°)] = S_2'/S_1'$ where θ increases counterclockwise and 0 corresponds to the horizontal positive direction. Note that the shallow diagonal traces observed in Figs. S4 and S5 arise from an artefact due to the use of neutral density filters in the detection path.

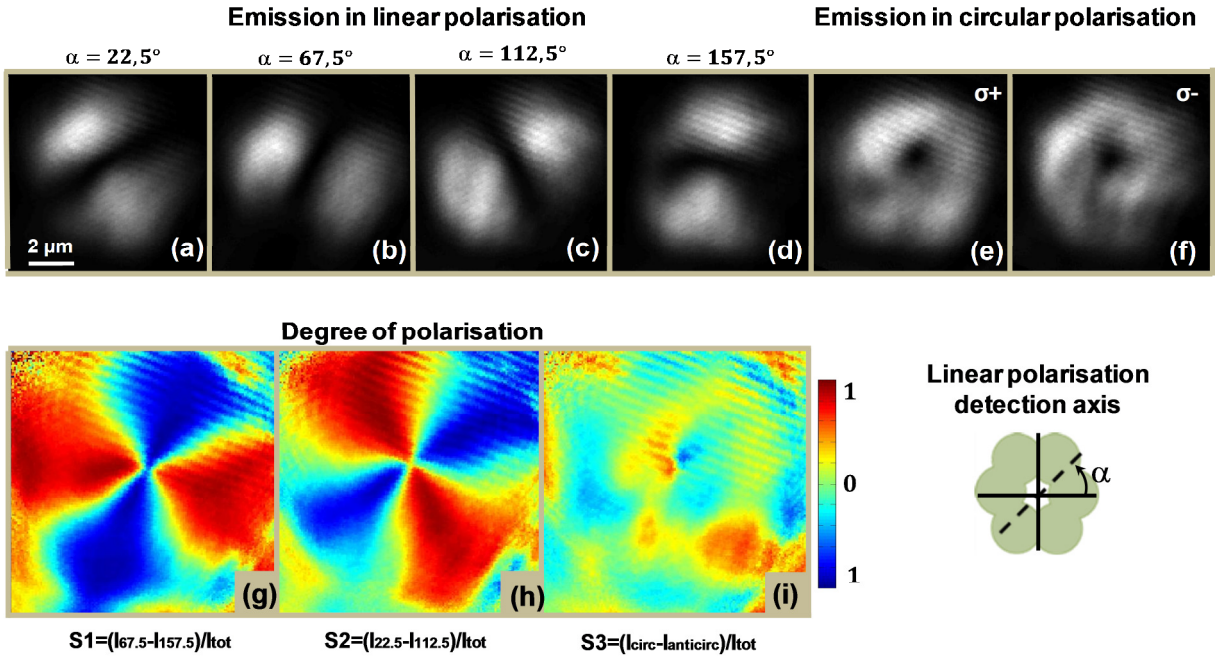

Figure S4. Linear polarization tomography of the $n = 1$ condensed state shown in Fig. 4 of the main text. From the degree of linear polarisation reported in (g)-(h), we extract the linear polarization direction for each point of the molecule, as shown in Fig. 4g.

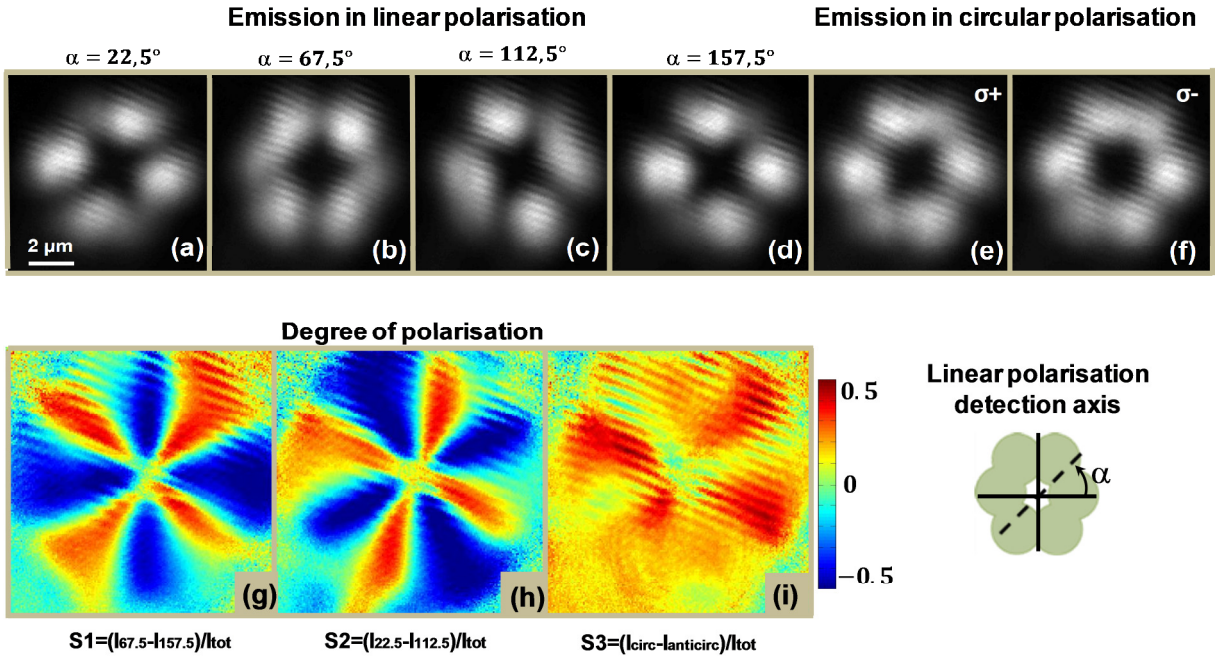

Figure S5. Linear polarization tomography of the $n = 2$ condensed state shown in Fig. 5 of the main text. From the degree of linear polarisation reported in (g)-(h), we extract the linear polarization direction for each point of the molecule, as shown in Fig. 5g.

E Level splitting under spatially inhomogeneous pumping

The origin the doublets visible in Fig. 3d-f is the fluctuation in the spatial position of the pump spot when changing the power of the excitation beam. The motorized stage controlling the input power induces a slight spatial shift of the pump spot with respect to the center of the structure. This shift creates an inhomogeneous excitonic reservoir distribution around the molecule. The interaction between the reservoir and the polaritons shifts the polariton energy locally proportional to the reservoir density [2]. Therefore, in this situation, the eigenstates are no longer those depicted in Fig. 2, which were calculated assuming identical onsite energies for all the micropillars. Instead, the eigenstates are deformed and condensation takes place in states oriented along and perpendicular to the offset direction and with different energies. Slight movements of the pump spot during the power dependence give rise to this phenomenon and to the appearance of doublets in the spectra shown in Fig. 3d-f.

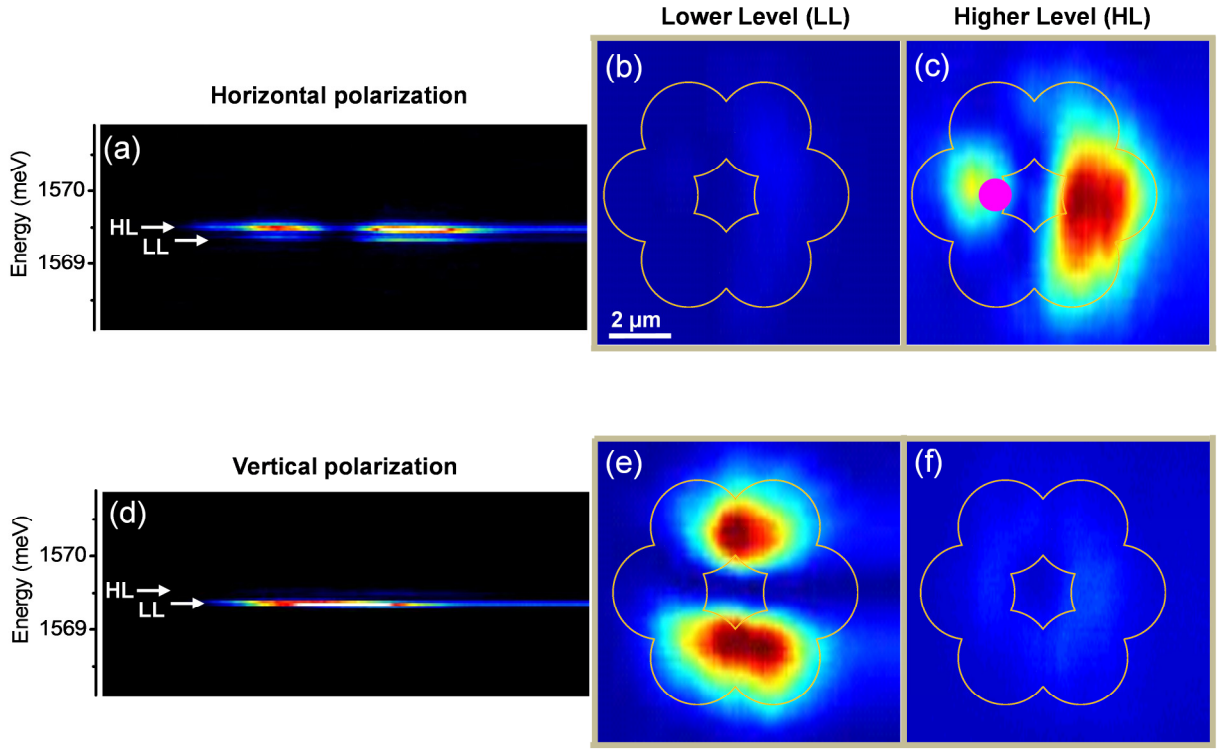

Figure S6. Photoluminescence of the $E(1)$ multiplet under dis-symetrized pump excitation at 84 mW. The localtion of the center of the Gaussian pump spot (FWHM 10 µm) is shown in (c). (a) Emission spectrum for horizontally polarized emission. A doublet is visible. Giving rise to the spatial patterns shown in (b) and (c). (d)-(f) Analogous to (a)-(c) for vertically polarized detection.

In order to prove this, we have measured the spatial distribution of the two substates for an intentional offset of the pump spot position with respect to the center of the photonic molecule. This situation is shown in Fig. S6, for condensation in level $E(1)$ at 84 mW of pump intensity. The situation corresponds to that of Fig. 4 except that in the case considered here the center of the spot was moved to the position marked with a pink dot in Fig. S6(c). In this case condensation takes place simultaneously in two substates labelled HL and EL in Fig. S6(a) and (d). By performing a spectrally resolved detection we map out the spatial

shape of the emission from each level, shown in Fig. S6(b), (c), (e) and (f). The emission from the higher level is mainly polarized in the horizontal polarization, while that of the lower level is vertical. This is consistent with a deformation of the potential of the molecule in the horizontal direction, as expected from the asymmetry of the injected reservoir, which is denser close to the pink dot due to the Gaussian profile of the excitation spot.

Note that the images shown in the condensation regime in Figs. 4 and 5 of the main text, where recorded under symmetric pumping of the molecule, with the pump laser spot perfectly aligned with the center of the molecule. In this situation, the blueshift induced by the reservoir is perfectly homogeneous, and the eigenstates of the system are well described by our model, which assumes identical micropillar energy. This is confirmed by the spatial homogeneity of the emission in Figs. 4g and 5g, and the monochromatic emission shown in Figs. 4h and 5h.

F Maxwell's equations simulations

The fine structure splitting, the level ordering and the polarization patterns predicted by the tight-binding model (see full description in Supplementary Section I), can be independently studied in our structure by performing finite elements simulations of Maxwell's equations. We can do this using COMSOL in the approximation of infinitely long waveguides. We thus simulate six overlapping waveguides whose transverse shape and dimensions are the same as the overlapping micropillars we have fabricated. The waveguides are described as perfect dielectrics with a refractive index of *n=3.54* (that of GaAs at 10K), surrounded by air (*n=1*). The simulations are done for a frequency of the electromagnetic waves corresponding to the wavelength of the lowest energy photonic mode of a single micropillar. We calculate the effective refractive index of the transverse electromagnetic eigenmodes [5] and retrieve their polarization and intensity pattern.

Figure S7 shows the calculated electric field amplitude and direction of the eigenmodes of the multiplets $E(1)$ and $E(2)$ along with the splittings for the polariton modes taking into account the photonic component of the polariton at a photon-exciton detuning of -5meV. The level ordering is the same as that in the tight binding model assuming $\hbar\Delta t > \Delta E$. The linear polarization patterns of the lowest energy modes of each multiplet (given by the arrow direction), coincide with those observed experimentally in Figs. 4 and 5. From the splittings ΔE_{SO} in the two multiplets calculated from the finite element simulation we can estimate the values of $\hbar\Delta t$ and ΔE:

$$\hbar\Delta t = \frac{1}{4}\left(\Delta E_{SO}(|l| = 1) - \Delta E_{SO}(|l| = 2)\right) = 6\ \mu\text{eV}$$

$$\Delta E = \frac{1}{4}\left(\Delta E_{SO}(|l| = 1) + \Delta E_{SO}(|l| = 2)\right) = 5\ \mu\text{eV}$$

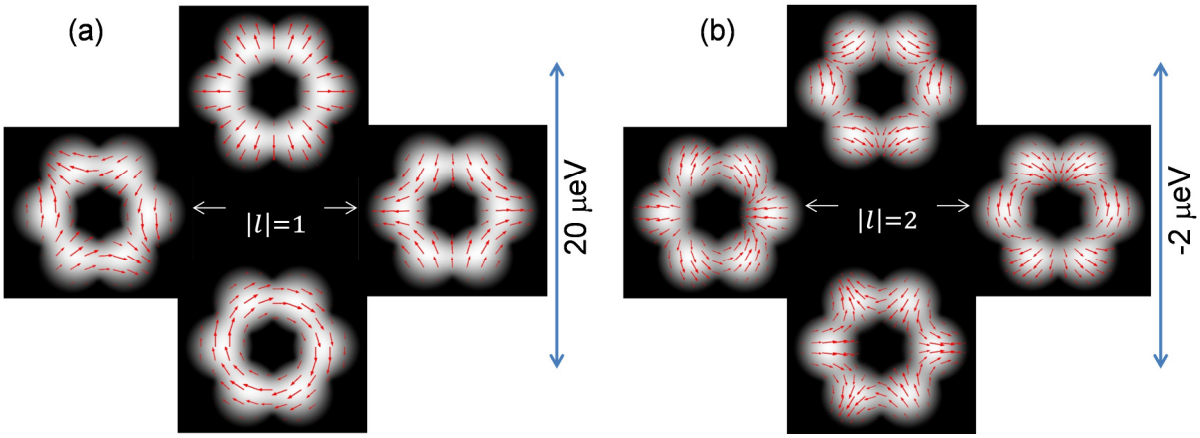

Figure S7. Intensity distribution (grey scale) and instantaneous electric field direction (arrows) calculated from a finite element simulation of Maxwell's equations for the geometry of our structure for the mutiplets corresponding to (a): $|l| = 1$ $[E(1)]$, and (b): $|l| = 2$ $[E(2)]$. The calculated splitting ΔE_{SO} between the upper and lowest substates of the multiplet is shown for the polariton modes, taking into account the photonic weight of the wavefunction for the photon-exciton detuning under consideration.

G Condensation kinetics

In our structure, we observe two condensation thresholds at two different excitation powers, as shown in Fig. 3 of the main text.

In an open-dissipative system with pumping and lifetime the Bose Einstein condensation does not necessarily occur in the ground state since relaxation kinetics and nonlinear effects have to be taken into account [6, 7]. Within the simplest approximation, the equation describing the occupation of a confined state can be written in the form:

$$\frac{dN}{dt} = W_{in}\left(N+1\right) - N\left(W_{out}+1/\tau\right), \qquad \text{(B)}$$

where τ is the state lifetime. $W_{in,out}$ are the scattering rates toward and outward the state. They verify:

$$W_{in} = W_{out}e^{-E/k_bT} = WY_{cR}e^{-E/k_bT},$$

where, E is the energy of the considered state, Y_{cR} is the overlap integral between the state density and the exciton reservoir distribution. W depends on the system parameters, but

since the main relaxation mechanism is based on exciton-exciton interaction, W is a growing function of the carrier density and of the pumping power. Equation (B) can be recast as:

$$\frac{dN}{dt} = W_{in}\left(N+1\right) - N\left(\tilde{W}_{out}\right)$$

where

$W_{in} = \tilde{W}_{out} e^{-E'/k_bT} = WY_{cR} e^{-E/k_bT}$ which yields

$$E' = E + k_bT \ln\left(1 + \frac{1}{WY_{cR}\tau}\right) \qquad \text{(C)}$$

W, Y and τ are in general functions of E. The meaning of the previous development is that the state occupation in our pump-dissipative system can be expressed as thermal-like distribution function if one defines a new energy scale that includes the effect of particle life time. This is what is expressed in Eq. (C), where we can see that the state with the lowest effective energy E' is not necessarily the original ground state of the system. For instance, an excited state with a long lifetime τ can become the state with lowest effective E', and thus, the most favored for condensation to take place. The exact value of E' depends on the relaxation efficiency, pumping power, overlap integral between the reservoir and the state, lifetime. In the rest of the text we are going to analyze which is the most favored state in the molecule depending on the excitation conditions. The increase of W with pumping reduces the impact of the kinetics on the determination of the ground state.

Lifetime. As a first approximation, the polariton lifetime in this system depends on the absolute value of the angular momentum. Indeed, the decay of the particles is given by the extension of the wave function out of the structure. This extension is maximal for bound states with $l = 0$, it decreases for higher values of l and it is minimal for the anti-bound states [8] $l = 3$, with a variation which we estimated numerically of the order of 20 %. As a result, condensation in states with $l = 0$ is not favored by kinetics because of their short lifetime.

There are two additional mechanisms that result in the increase of the polariton lifetime with increasing energy. First of all the exciton content increases with energy, resulting in an enhanced lifetime. Second, the wavefunction of higher energy modes presents zeroes at the constrictions between the pillars, where the density of structural defects is higher. Thus, higher energy modes are more protected against the non-radiative losses associated to defects. The combination of these effects would result in condensation in the $E(3)$ energy level with the lowest threshold. However, to find the state in which condensation first takes

place, we need to additionally take into account the overlap of the considered state with the reservoir and the polariton interactions.

Overlap with the reservoir, spin-anisotropic interaction. The spin-anisotropic interaction of polaritons makes it energetically favorable for a condensate to be linearly polarized [9]. On the other hand, linear combination of states resulting in amplitude inhomogeneities show a reduced overlap with the excitonic reservoir, which is homogeneous all over the molecule in our excitation conditions. Thus, the $l = 3$ [$E(3)$] state is not favored as its wavefunction has zeros in between the pillars [see Fig. 1(d)]. Linear combinations of the non-split states of the $|l| = 1$ and $|l| = 2$ multiplets (marked with arrows in Fig. S7) give rise to circularly polarized emission components and spatial inhomogeinities, and are thus also unfavored. For these reasons, the states which favor condensation are the linearly polarized, spatially homogeneous split states of the $|l| = 1$ and $|l| = 2$ multiplets.

At low pumping, condensation is expected to occur in the most kinetically favored states (with higher lifetime), namely the two split states of the multiplet $|l| = 2$. The choice between the upper and lowermost of the two is more subtle. Although the spatial distributions of the levels of the multiplet look very similar in Fig. S7(b), they present slight differences. The difference arises from the penetration of the electromagnetic field out of the micropillars, which depends on the local orientation of the polarisation close to the edge of the structure. As the upper and lowermost level hold very different polarisation textures, their wavefunctions present spatial differences. Thus, the overlap with the reservoir of these two modes is slightly different. Additionally, the energy difference between the substates might result in different relaxation rates. These effects, though being small, are enough to trigger condensation in the observed states. This situation, in a planar microcavity context, has been recently studied from a theoretical point of view in [7].

Going to higher power, the depletion of the reservoir and the interactions modify the relaxation rates described by $Y_{cR}\,W$ in Eq. (C). The effective energies of the state evolve and the effective ground state becomes the lowest of the two split states in the multiplet $|l| = 1$, namely, the state with an azimuthal polarization. For the same reasons considered in the previous paragraph, condensation is triggered in the lowermost state.

Numerical simulations. In order to confirm this finding, we use a model based on self-consistent coupled semi-classical Boltzmann and nonlinear Schrödinger equations containing Eqs. (B) and (C) [2], and find a good agreement with the experimental results.

To carry out a direct comparison with the experiment, we calculate the emission from the quantized states of the hexagonal molecule in the reciprocal space, taking into account the occupation numbers found from the simulations described above. The results are shown in Fig. S8. Below threshold (left panel), all states are approximately equally populated. Main emission comes from the ground state which can be identified by a maximum of emission at $k = 0$. At higher pumping (right panel), condensation occurs at the most favored state at this

power which, in the case represented in Fig. S8-right, is the state with $|l| = 1$ and azimuthal polarization. The emission from this state dominates the spectrum.

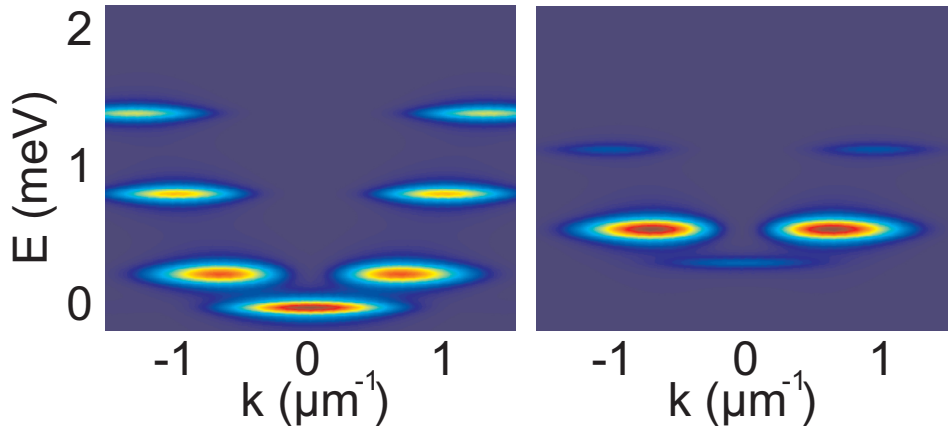

Figure S8. Simulated emission pattern in the reciprocal space below (left panel) and above threshold (right panel). Condensation occurs in the lowest state of the $|l| = 1$ multiplet, with an azimuthal polarization pattern.

H Spin-Orbit Hamiltonian in operator and effective field forms

Hamiltonians (3) and (4) in the main text can be expressed in the form of an operator acting on a spinor $\vec{\psi}(j) = [\psi^+(j), \psi^-(j)]^T$, with $j = 1, \dots, 6$ the micropillar index and +,- the two elements of the circular polarisation basis. For this purpose we introduce the diagonal part of the spinor Hamiltonian $\widehat{H}_0 = \widehat{H}(\Delta t = 0,\ \Delta E = 0)$. Eigenstates of $\widehat{H}_0$ are described by the quantum number l:

$$E(l, \sigma) = -2\hbar t\ cos(2\pi l/6)$$

We can introduce an operator $\widehat{M} = \frac{\partial^2 E}{\partial l^2} = cos(2\pi l/6)$ allowing us to write the complete Hamiltonian:

$$\widehat{H} = \widehat{H}_0 - \frac{\Delta E}{2}\begin{pmatrix} 0 & e^{-2i\varphi_j} \\ e^{2i\varphi_j} & 0 \end{pmatrix} - \frac{\hbar \Delta t}{2}\left[\widehat{M}\begin{pmatrix} 0 & e^{-2i\varphi_j} \\ e^{2i\varphi_j} & 0 \end{pmatrix} + \begin{pmatrix} 0 & e^{-2i\varphi_j} \\ e^{2i\varphi_j} & 0 \end{pmatrix}\widehat{M}\right],$$

where $\varphi_j = j\pi/3$.

In the context of SO coupling in semiconductors, it is meaningful to express the Hamiltonian in terms of an effective magnetic field acting on the spin of the particles. In the case of Hamiltonian (3)-(4), this can be done in cylindrical coordinates in the following way:

$$\epsilon\vec{\psi} = -\frac{\hbar^2}{2mR^2}\frac{\partial^2}{\partial\varphi^2}\vec{\psi} - \vec{\Omega}\cdot\vec{\psi}$$

where R is the mean radius of the molecule and $\vec{\Omega}$ is the effective field:

$$\frac{\hbar\vec{\Omega}}{2} = \left(\frac{\hbar\,\Delta t}{2}cos\left(\frac{\pi k}{3}\right) + \frac{\Delta E}{2}\right)\begin{pmatrix} 0 & e^{-2i\varphi_j} \\ e^{2i\varphi_j} & 0 \end{pmatrix}.$$

The polarisation patterns in the eigenmodes can then be understood as those arising from the alignment and antialignement of the photon pseudospin with respect to the effective field $\vec{\Omega}$.

Supplementary references

[1] D. Bajoni, P. Senellart, E. Wertz, et al., Phys. Rev. Lett. 100, 047401 (2008).

[2] M. Galbiati, L. Ferrier, D. D. Solnyshkov, et al., Phys. Rev. Lett. 108, 126403 (2012).

[3] T. Jacqmin, I. Carusotto, I. Sagnes, et al., Phys. Rev. Lett. 112, 116402 (2014).

[4] M. Born and E. Wolf, *Principles of optics electromagnetic theory of propagation, interference and diffraction of light* (Pergamon, Oxford, 1980).

[5] B. E. A. Saleh and M. C. Teich, *Fundamentals of Photonics* (John Wiley & Sons, New York, 2007).

[6] D. Sanvitto, A. Amo, L. Vina, et al., Phys. Rev. B 80, 045301 (2009).

[7] L. Ge, A. Nersisyan, B. Oztop, et al., arXiv:1311.4847v1 (2013).

[8] I. L. Aleiner, B. L. Altshuler, and Y. G. Rubo, Phys. Rev. B 85, 121301 (2012).

[9] I. A. Shelykh, Y. G. Rubo, G. Malpuech, et al., Phys. Rev. Lett. 97, 066402 (2006).

Supplementary Information for "Spin-orbit coupling for photons and polaritons in microstructures" I.- Tight binding model

V. G. Sala,[1,2] D. D. Solnyshkov,[3] I. Carusotto,[4] T. Jacqmin,[1] A. Lemaître,[1] H. Terças,[3] A. Nalitov,[3] M. Abbarchi,[1,5] E. Galopin,[1] I. Sagnes,[1] J. Bloch,[1] G. Malpuech,[3] and A. Amo[1]

[1] *Laboratoire de Photonique et Nanostructures, CNRS/LPN, Route de Nozay, 91460 Marcoussis, France*
[2] *Laboratoire Kastler Brossel, Université Pierre et Marie Curie, École Normale Supérieure et CNRS, UPMC Case 74, 4 place Jussieu, 75252 Paris Cedex 05, France*
[3] *Institut Pascal, PHOTON-N2, Clermont Universit, Universit Blaise Pascal, CNRS, 24 avenue des Landais, 63177 Aubire Cedex, France*
[4] *INO-CNR BEC Center and Dipartimento di Fisica, Università di Trento, I-38123, Povo, Italy*
[5] *Laboratoire Pierre Aigrain, École Normale Supérieure, CNRS (UMR 8551), Université P. et M. Curie, Université D. Diderot, 75005 Paris, France*

(Dated: January 8, 2015)

I. TIGHT-BINDING DERIVATION OF THE SPIN-ORBIT HAMILTONIAN OF PHOTONIC BENZENE

In this section we present the tight-binding derivation of the spin-orbit Hamiltonians (3) and (4) of the main text. We consider a chain of cylindrical micropillar cavities arranged at the vertices of a regular polygon of M sides, as sketched in Fig. 1 for the $M = 6$ case of the benzene experiments. The polygon is assumed to sit on the $x - y$ plane.

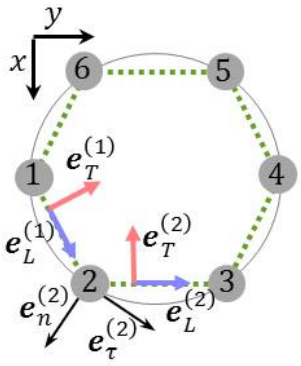

FIG. 1. Sketch of the system under consideration.

On each site, a single orbital mode is available, with an approximately cylindrically symmetric wavefunction. Each orbital mode has a twofold spin degeneracy corresponding to the two polarization directions on the x and y directions. On the jth site centered at position $\mathbf{R}_j$, the vector electric (or polaritonic) field operator has the form:

$$\hat{\vec{\mathbf{E}}}(\mathbf{r}) = \phi(\mathbf{r}-\mathbf{R}_j)[\mathbf{e}_x\hat{a}_{j,x} + \mathbf{e}_y\hat{a}_{j,y}] = \\ = \phi(\mathbf{r}-\mathbf{R}_j)[\mathbf{e}_{\sigma_+}\hat{a}_{j,\sigma_+} + \mathbf{e}_{\sigma_-}\hat{a}_{j,\sigma_y}], \quad (1)$$

where the $\hat{a}_x$, $\hat{a}_y$ and $\hat{a}_{\sigma_+}$, $\hat{a}_{\sigma_-}$ are two among the possible basis on which the vector electric field can be expanded. $\mathbf{e}_{x,y}$ is a cartesian basis, while $\mathbf{e}_{\sigma_\pm} = (\mathbf{e}_x \pm i\mathbf{e}_y)/\sqrt{2}$ is the circular basis.

In the following, it will be convenient to use the compact and basis-independent vector notation

$$\hat{\mathbf{a}}_i = \mathbf{e}_x\hat{a}_{j,x} + \mathbf{e}_y\hat{a}_{j,y} = \mathbf{e}_{\sigma_+}\hat{a}_{j,\sigma_+} + \mathbf{e}_{\sigma_-}\hat{a}_{j,\sigma_y}. \quad (2)$$

For both the cartesian and the circular basis, the commutators satisfy bosonic commutation rules.

For each link connecting the $j \to j+1$ sites, we can define the real unit vectors $\mathbf{e}_L^{(j)}$ and $\mathbf{e}_T^{(j)}$ respectively parallel and orthogonal to the link direction $\mathbf{R}_{i+1} - \mathbf{R}_i$. The main assumption of our model is that tunneling along the $j \to j+1$ link occurs with different amplitudes t_L and t_T for photons polarized along the $\mathbf{e}_L^{(i)}$ and $\mathbf{e}_T^{(i)}$ directions, respectively. For the moment, we will not consider the onsite splitting ΔE.

In second quantization terms, the many-body Hamiltonian then reads:

$$H = -\sum_{j=1}^{M}\{[\hbar t_L(\hat{\mathbf{a}}_{j+1}^\dagger \cdot \mathbf{e}_L^{(j)})(\mathbf{e}_L^{(j)\dagger} \cdot \hat{\mathbf{a}}_j) + \\ + \hbar t_T(\hat{\mathbf{a}}_{j+1}^\dagger \cdot \mathbf{e}_T^{(j)})(\mathbf{e}_T^{(j)\dagger} \cdot \hat{\mathbf{a}}_j)] + \text{h.c.}\}. \quad (3)$$

Physically, the $\mathbf{e}_{L,T}^{(j)\dagger} \cdot \hat{\mathbf{a}}_j$ expression selects the component of the vector $\hat{\mathbf{a}}_j$ field on the jth side along the $\mathbf{e}_{L,T}^{(j)}$ unit vector. Given the periodic boundary conditions of the system, in the sum the $(M+1)$th site has to be identified with the 1st and the 0th with the Mth.

As the many-body Hamiltonian (3) does not involve any interaction terms, it is straightforward to derive a Schrödinger equation for the single-particle $\mathbb{C}$-number vector wavefunction $\boldsymbol{\alpha}_j$ that defines states on the one-body subspace:

$$|\psi_1\rangle = \sum_j [\boldsymbol{\alpha}_j \cdot \hat{\mathbf{a}}_j^\dagger]|\text{vac}\rangle \quad (4)$$

As usual, the Schrödinger equation can be obtained from

the Heisenberg equation for the field operators $\hat{\mathbf{a}}_j$

$$i\hbar\frac{d}{dt}\hat{\mathbf{a}}_j = [\hat{\mathbf{a}}_j, H] \tag{5}$$

by replacing the field operators $\hat{\mathbf{a}}_j$ with the one-body wavefunction $\boldsymbol{\alpha}_j$. In this way, one obtains

$$i\frac{d\boldsymbol{\alpha}_j}{dt} = t_L\mathbf{e}_L^{(j-1)}(\mathbf{e}_L^{(j-1)\dagger}\cdot\boldsymbol{\alpha}_{j-1}) + t_T\mathbf{e}_T^{(j-1)}(\mathbf{e}_T^{(j-1)\dagger}\cdot\boldsymbol{\alpha}_{i-1}) + \\ + t_L\mathbf{e}_L^{(j)}(\mathbf{e}_L^{(j)\dagger}\cdot\boldsymbol{\alpha}_{j+1}) + t_T\mathbf{e}_T^{(j)}(\mathbf{e}_T^{(j)\dagger}\cdot\boldsymbol{\alpha}_{j+1}). \tag{6}$$

If M is even, the symmetry operation $\mathcal{S}$ defined as:

$$\mathcal{S}^\dagger\hat{\mathbf{a}}_j\mathcal{S} = (-1)^j\hat{\mathbf{a}}_j \tag{7}$$

anticommutes with the Hamiltonian

$$\mathcal{S}^\dagger H\mathcal{S} = -H. \tag{8}$$

As a result, if $|\psi\rangle$ is an eigenstate of the Hamiltonian H of energy E, then $\mathcal{S}|\psi\rangle$ is an eigenstate of opposite energy $-E$. At the single-particle level, the action of the operator S is to invert the sign of the field on the odd sites

$$(\mathcal{S}\boldsymbol{\alpha})_j = (-1)^j\boldsymbol{\alpha}_j, \tag{9}$$

so that the tunneling energy of each link changes sign.

The standard translation operator T is defined as

$$T^\dagger\hat{\mathbf{a}}_jT = \hat{\mathbf{a}}_{j+1}: \tag{10}$$

physically, the photon field on the translated state $T|\psi\rangle$ at site j is equal to the original field on the site $j+1$. In the general case $t_L \neq t_T$, the operator T does not commute with the Hamiltonian: translation changes the relative orientation of the photon field $\hat{\mathbf{a}}_j$ with respect to the link frame defined by the pair $\mathbf{e}_{L,T}^{(j)}$.

One has to define a new translation operator $\tilde{T}$ as follows

$$\tilde{T}^\dagger\hat{\mathbf{a}}_j\tilde{T} = \mathcal{R}_{-2\pi/M}\hat{\mathbf{a}}_{j+1}: \tag{11}$$

translation by one site has to be combined with a rotation by an angle $-2\pi/M$ so to compensate the different orientation of the link. This new operator $\tilde{T}$ commutes with the Hamiltonian H. It is immediate to check that after a full round trip around the chain, it gives back the identity $\tilde{T}^M = \mathbf{1}$. In physical terms, the operator $\tilde{T}$ describes discrete rotations by $2\pi/M$ around the chain, and therefore corresponds to the *total* angular momentum of the state.

Let's now restrict to the single-particle space. As $\tilde{T}$ commutes with H, eigenstates can be found with well defined quantum number k as compared to generalized translations, that is, such that

$$\tilde{T}|\psi\rangle = e^{2\pi ik/M}|\psi\rangle \tag{12}$$

with $k = 1, \ldots, M$. It is important to note that the wavevector k does not straightforwardly correspond to the orbital part of the angular momentum. This is easy to see on $\sigma_\pm$ circularly polarized states such that

$$\boldsymbol{\alpha}_j = \alpha_j\begin{pmatrix}1\\ \pm i\end{pmatrix}. \tag{13}$$

In this case, if the wavefunction has orbital angular momentum $l\cdot 2\pi/6$ (again $l = 1, \ldots, M$), its orbital part takes the form $\alpha_j = \alpha_o e^{ijl2\pi/6}$. Thus, the complete wavefunction is:

$$\boldsymbol{\alpha}_j = \alpha_o e^{ijl2\pi/6}\begin{pmatrix}1\\ \pm i\end{pmatrix}, \tag{14}$$

which contains a spin contribution ± 1, and total angular momentum $k = l \pm 1$. On the other hand, an experiment where $\sigma_\pm$ light is selected, is sensitive to the orbital wavefunction only.

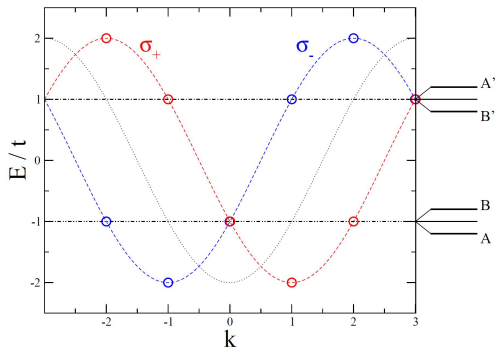

FIG. 2. Sketch of the eigenstates of a $M = 6$ photonic hexagonal molecule. Red (blue) points indicate the σ_+ (σ_-) polarized states. States are labeled in terms of the total angular momentum k.

Let's begin to diagonalize H in the $t_L = t_T = t$ case. In this case, on each site one has

$$\mathbf{e}_L^{(j)}\times\mathbf{e}_L^{(j)\dagger} + \mathbf{e}_T^{(j)}\times\mathbf{e}_T^{(j)\dagger} = \mathbf{1}. \tag{15}$$

The energy of the state is therefore given by the orbital energy only, equal to

$$E_l = -2\hbar t\,\cos(2\pi l/M). \tag{16}$$

Even though the spin decouples from the orbital motion, it is instructive to see the behavior of the generalized translation operators $\tilde{T}$. The circularly polarized states are eigenstates of the rotation operator

$$\mathcal{R}_\theta\sigma_\pm = e^{-i\theta}\sigma_\pm. \tag{17}$$

As a result, the energy of $\sigma = \sigma_\pm$ polarized states of total angular momentum k is

$$E(k,\sigma) = -2\hbar t\,\cos[2\pi(k-\sigma)/M] \tag{18}$$

and its dispersion is sketched in Fig. 2. The presence of a spin-orbit coupling term is apparent in (18), where the dispersion of the $\sigma_\pm$ is laterally shifted by $\Delta k = \pm 1$. In Hamiltonian terms, we can write

$$H = \sum_{k,\sigma} E(k,\sigma)\, \hat{b}^\dagger_{k,\sigma}\, \hat{b}_{k,\sigma}, \tag{19}$$

where

$$\hat{b}_{k,\sigma} = \frac{1}{\sqrt{M}} \sum_j e^{-2\pi i (k-\sigma) j/M} \hat{a}_{j,\sigma} \tag{20}$$

is the destruction operator for a photon of total angular momentum k and spin σ

In the general case $t_L \neq t_T$, the orbital angular momentum l is no longer a good quantum number, but k remains so: the $t_L - t_T$ coupling does not break rotational invariance. To qualitatively understand the degeneracies of the eigenstates in the experimentally relevant case $|t_L - t_T| \ll t_{L,T}$ it is useful to draw the dispersion of the $\sigma_\pm$ states as a function of k and include the effect of $t_L - t_T$ only at the crossing points of the bands. As one can see in Fig. 2, for even values of M such crossings only occur at $k = 0, M/2$. For all other values, the bands are non-degenerate.

As a result, the ground state is two-fold degenerate and is spanned by the eigenstates $|\sigma_+, k = 1\rangle$ and $|\sigma_-, k = -1\rangle$ (as usual, because of the discrete rotational symmetry the quantum number k is only defined modulo M, so $k = -1$ is equivalent to $k = M - 1$). Its energy is $\simeq -2t$. Correspondingly, thanks to the $\mathcal{S}$ symmetry mentioned above (the $\mathcal{S}$ operation sends a state with orbital momentum l into a state of orbital momentum $l + M/2$), the highest energy state is two-fold degenerate at energy $\simeq 2\hbar t$ and is spanned by $|\sigma_+, k = M/2 + 1\rangle$ and $|\sigma_-, k = -M/2 - 1\rangle$.

The first excited manifold at $E \simeq -2\hbar t \cos(2\pi/M) = -\hbar t$ is four-fold degenerate for $t_L = t_T$. The two external states $(\sigma_+, k = 2)$ and $(\sigma_-, k = -2)$ have no other available state at the same k, so remain degenerate at $E = -\hbar t$. On the otehr hand, the two other states $|\sigma_+, k = 0\rangle$ and $|\sigma_-, k = 0\rangle$ can be mixed by the angular momentum conserving $t_L - t_T$ terms.

To understand the form of the new eigenstates, it is useful to give an explicit expression for the $\Delta t = t_L - t_T$ terms in the $\sigma_\pm$ basis; from now on we will assume for clarity $\Delta t > 0$. Rewriting the Hamiltonian

$$\begin{aligned} H = -\sum_{j=1}^{M} \{ & \hbar t [\hat{\mathbf{a}}^\dagger_{j+1} \hat{\mathbf{a}}_j + \hat{\mathbf{a}}^\dagger_j \hat{\mathbf{a}}_{j+1}] + \\ & + \frac{\hbar \Delta t}{2} [(\hat{\mathbf{a}}^\dagger_{j+1} \cdot \mathbf{e}^{(j)}_L)(\mathbf{e}^{(j)\dagger}_L \cdot \hat{\mathbf{a}}_j) + \\ & - (\hat{\mathbf{a}}^\dagger_{j+1} \cdot \mathbf{e}^{(j)}_T)(\mathbf{e}^{(j)\dagger}_T \cdot \hat{\mathbf{a}}_j)] + \text{h.c.}\}. \end{aligned} \tag{21}$$

and expressing it in terms of the k-space operators, one gets to

$$\begin{aligned} H = & -\sum_{j=1}^{M} \{\hbar t [\hat{\mathbf{a}}^\dagger_{j+1} \hat{\mathbf{a}}_j + \hat{\mathbf{a}}^\dagger_j \hat{\mathbf{a}}_{j+1}] + \\ & - \hbar \Delta t \sum_k \cos(\frac{2\pi k}{6})\, [\hat{b}^\dagger_{k,\sigma_-} \hat{b}_{k,\sigma_+} e^{-4\pi i/M} + \text{h.c.}]. \end{aligned} \tag{22}$$

From this expression it is immediate to see that the Δt term still conserves angular momentum and that the $|\sigma_+, k = 0\rangle$ and $|\sigma_-, k = 0\rangle$ give rise to new eigenstates at energies $E \simeq -2\hbar t \cos(2\pi/M) \pm \hbar \Delta t$. Given the phase factor in the last term of (22), the lowest eigenstate at energy $-2\hbar t \cos(2\pi/M) - \hbar \Delta t$ is of the form

$$|\psi^{(A)}\rangle = \frac{1}{\sqrt{2}} [e^{2\pi i/M} |0, \sigma_+\rangle + e^{-2\pi i/M} |0, \sigma_-\rangle], \tag{23}$$

while the highest at energy $-2\hbar t \cos(2\pi/M) + \hbar \Delta t$ has the form

$$|\psi^{(B)}\rangle = \frac{1}{\sqrt{2}} [e^{2\pi i/M} |0, \sigma_+\rangle - e^{-2\pi i/M} |0, \sigma_-\rangle]. \tag{24}$$

These are the upper and lower states sketched in Fig. 2(f) of the main text. It is interesting to get insight on the spatial polarization structure of the $|\psi_{A,B}\rangle$ states. Replacing the explicit expression of the $|0, \sigma_\pm\rangle$ states, one obtains for the lower A state

$$\begin{aligned} \psi^{(A)}_j = \frac{1}{2} [e^{-2\pi i (j-1)/M} \begin{pmatrix} 1 \\ i \end{pmatrix} + e^{2\pi i (j-1)/M} \begin{pmatrix} 1 \\ -i \end{pmatrix}] = \\ = \begin{pmatrix} \cos(2\pi(j-1)/M) \\ \sin(2\pi(j-1)/M) \end{pmatrix} \end{aligned} \tag{25}$$

which is an azymuthal polarization: For instance, for $j = 1$ the polarization is vertical (note the axis convention in Fig. 1). Analogously for the higher B state,

$$\begin{aligned} \psi^{(B)}_j = \frac{1}{2} [e^{-2\pi i (j-1)/M} \begin{pmatrix} 1 \\ i \end{pmatrix} - e^{2\pi i (j-1)/M} \begin{pmatrix} 1 \\ -i \end{pmatrix}] = \\ = i \begin{pmatrix} -\sin(2\pi(j-1)/M) \\ \cos(2\pi(j-1)/M) \end{pmatrix} \end{aligned} \tag{26}$$

which is a radial polarization. These features are visible in the polarization patterns of the different eigenstates that are plotted in Fig. 3. In particular, the A state is the one at $E = -1.002$ (we have used $\hbar t = 1$ and $\hbar \Delta t = 0.002$) on the third column (from left) of the top row. The B state is the one at $E = -0.998$.

The structure of the second highest energy manifold at $E = \hbar t$ (corresponding to Fig. 2(g) of the main text) is directly obtained via the $\mathcal{S}$ symmetry that sends the total angular momentum $k \to k + \pi/M$ while keeping the polarization pattern intact. As a result, the highest state A' of this manifold will have an azimuthal polarization, while the lowest one B' will have a radial polarization. This is again visible in Fig. 3 by comparing the states at $E = 1.002$ and $E = 0.998$.

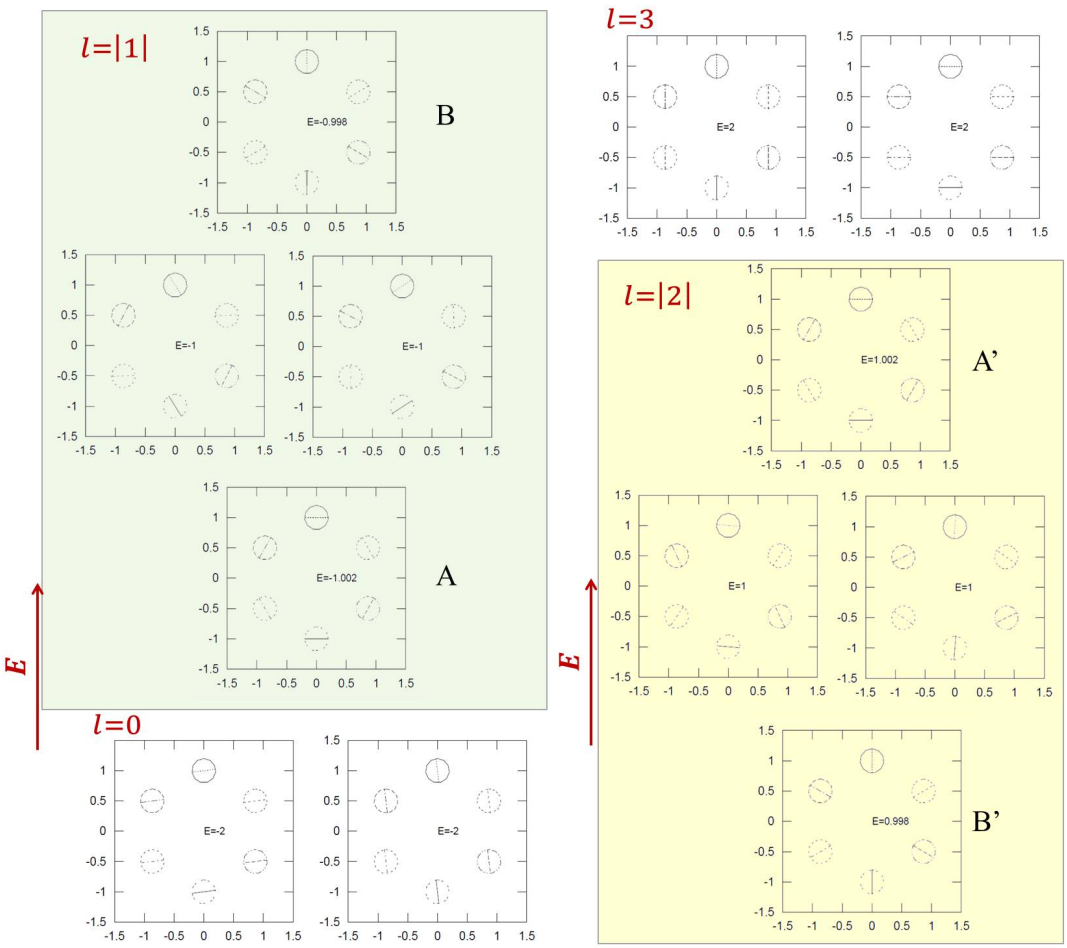

FIG. 3. Calculated polarization pattern for the different eigenstates of a photonic benzene molecule. Eigenstates are sorted for growing eigenenergy, indicated in the center of each panel (bottom-up on each column). The calculation is performed by diagonalizing the Hamiltonian (3) within the one-particle subspace. Parameters: $t_L = 1.001$, $t_T = 0.999$, $\Delta E = 0$.

In addition to the polarisation depenendent tunnelling we have considered up to now $(t_L - t_T)$ our photonic structures may show an onsite splitting $2\Delta E$ between modes linearly polarised azimuthal and radially with respect to the ring geometry, corresponding to vectors $\mathbf{e}_\tau^{(j)}$ and $\mathbf{e}_n^{(j)}$, respectively, in Fig. 1. This onsite splitting accounts for the waveguide shape of the structure. Formally, this splitting can be introduced in the tight-binding model by a Hamiltonian term of the form:

$$H_{\tau n} = -\Delta E \sum_{j=1}^{M} \{(\hat{\mathbf{a}}_j^\dagger \cdot \mathbf{e}_\tau^{(j)})(\mathbf{e}_\tau^{(j)\dagger} \cdot \hat{\mathbf{a}}_j) + - (\hat{\mathbf{a}}_j^\dagger \cdot \mathbf{e}_n^{(j)})(\mathbf{e}_n^{(j)\dagger} \cdot \hat{\mathbf{a}}_j)\}. \quad (27)$$

Expressing it in terms of the k-space operators, one gets a term of the form

$$H_{\tau n} = -\Delta E \sum_k [\hat{b}_{k,\sigma_-}^\dagger \hat{b}_{k,\sigma_+} e^{-4\pi i/M} + \text{h.c.}] \quad (28)$$

with exactly the same form as the Δt correction in (22). Equation (28) thus takes the form:

$$H = -\sum_{j=1}^{M} \hbar t[\hat{\mathbf{a}}_{j+1}^\dagger \hat{\mathbf{a}}_j + \hat{\mathbf{a}}_j^\dagger \hat{\mathbf{a}}_{j+1}] + -\sum_k \left(\hbar \Delta t \cos(\frac{2\pi k}{6}) + \Delta E\right) [\hat{b}_{k,\sigma_-}^\dagger \hat{b}_{k,\sigma_+} e^{-4\pi i/M} + \text{h.c.}]. \quad (29)$$

Consequently, the eigenstates maintain the same form with the replacement

$$\hbar \Delta t \cos\left(\frac{2\pi k}{6}\right) \to \hbar \Delta t \cos\left(\frac{2\pi k}{6}\right) + \Delta E. \quad (30)$$

Assuming $\hbar \Delta t > 0$, the lower A eigenstate of the $k = 0$ manifold remains azimuthally polarized as long as $\hbar \Delta t > -\Delta E$. The situation is slightly different for the $k = 3$ manifold, where the radially polarized state keeps a lower

energy as long as $\hbar\Delta t > \Delta E$. as sketched in the insets of Fig. 2(f)-(g) of the main text. The relative magnitude of the two effects has to be determined case by case on each specific structure. For instance, if instead of a hexagonal chain we would have a uniform ring guide, ΔE would be the dominant contribution to the SO coupling.

II. SPIN-ORBIT HAMILTONIAN IN MATRIX AND OPERATOR FORM

We can gain insights on the emergence of the spin-orbit coupling from the polarisation dependent tunneling and onsite splittings by doing a matricial treatment of the problem. We again consider the basis of single pillar states with polarisations oriented longitudinal ($\mathbf{e}_L$) and transverse ($\mathbf{e}_T$) to the link between j and $j+1$: $|j, L/T\rangle$. The polarisation dependent tunneling is described by single polariton Hamiltonian matrix elements:

$$\begin{aligned} t_L &= \left\langle j, L \left| \hat{H} \right| j+1, L \right\rangle \\ t_T &= \left\langle j, T \left| \hat{H} \right| j+1, T \right\rangle \end{aligned} \tag{31}$$

while

$$\left\langle j, L \left| \hat{H} \right| j+1, T \right\rangle = \left\langle j, L \left| \hat{H} \right| j+1, L \right\rangle = 0. \tag{32}$$

In order to include the onsite splitting between modes polarised in the direction radial and azimuthal to the ring geometry of the molecule, it is convenient to change to the polarisation basis n, τ depicted in Fig. 1:

$$\begin{aligned} |j, n\rangle &= \frac{\sqrt{3}}{2} |j, T\rangle - \frac{1}{2} |j, L\rangle \\ |j, \tau\rangle &= \frac{1}{2} |j, T\rangle - \frac{\sqrt{3}}{2} |j, L\rangle \\ |j+1, n\rangle &= \frac{\sqrt{3}}{2} |j+1, T\rangle - \frac{1}{2} |j+1, L\rangle \\ |j+1, \tau\rangle &= -\frac{1}{2} |j+1, T\rangle + \frac{\sqrt{3}}{2} |j+1, L\rangle . \end{aligned} \tag{33}$$

In this basis, the tight binding Hamiltonian reads:

$$\hat{H} = \begin{array}{c} \\ 1,n \\ 1,\tau \\ 2,n \\ 2,\tau \\ 3,n \\ 3,\tau \\ 4,n \\ 4,\tau \\ 5,n \\ 5,\tau \\ 6,n \\ 6,\tau \end{array} \begin{array}{c} \begin{array}{cccccccccccc} 1,n & 1,\tau & 2,n & 2,\tau & 3,n & 3,\tau & 4,n & 4,\tau & 5,n & 5,\tau & 6,n & 6,\tau \end{array} \\ \begin{pmatrix} E_n & 0 & -t_{nn} & t_{n\tau} & 0 & 0 & 0 & 0 & 0 & 0 & -t_{nn} & -t_{n\tau} \\ 0 & E_\tau & -t_{n\tau} & -t_{\tau\tau} & 0 & 0 & 0 & 0 & 0 & 0 & t_{n\tau} & -t_{\tau\tau} \\ -t_{nn} & -t_{n\tau} & E_n & 0 & -t_{nn} & t_{n\tau} & 0 & 0 & 0 & 0 & 0 & 0 \\ t_{n\tau} & -t_{\tau\tau} & 0 & E_\tau & -t_{n\tau} & -t_{\tau\tau} & 0 & 0 & 0 & 0 & 0 & 0 \\ 0 & 0 & -t_{nn} & -t_{n\tau} & E_n & 0 & -t_{nn} & -t_{n\tau} & 0 & 0 & 0 & 0 \\ 0 & 0 & t_{n\tau} & -t_{\tau\tau} & 0 & E_\tau & -t_{n\tau} & -t_{\tau\tau} & 0 & 0 & 0 & 0 \\ 0 & 0 & 0 & 0 & -t_{nn} & -t_{n\tau} & E_n & 0 & -t_{nn} & -t_{n\tau} & 0 & 0 \\ 0 & 0 & 0 & 0 & t_{n\tau} & -t_{\tau\tau} & 0 & E_\tau & -t_{n\tau} & -t_{\tau\tau} & 0 & 0 \\ 0 & 0 & 0 & 0 & 0 & 0 & -t_{nn} & -t_{n\tau} & E_n & 0 & -t_{nn} & t_{n\tau} \\ 0 & 0 & 0 & 0 & 0 & 0 & t_{n\tau} & -t_{\tau\tau} & 0 & E_\tau & -t_{n\tau} & -t_{\tau\tau} \\ -t_{nn} & t_{n\tau} & 0 & 0 & 0 & 0 & 0 & 0 & -t_{nn} & -t_{n\tau} & E_n & 0 \\ -t_{n\tau} & -t_{\tau\tau} & 0 & 0 & 0 & 0 & 0 & 0 & t_{n\tau} & -t_{\tau\tau} & 0 & E_\tau \end{pmatrix} \end{array}, \tag{34}$$

where the onsite energy splitting $\Delta E = E_n - E_\tau$, and

$$\begin{aligned} t_{nn} &= \frac{1}{4}(3t_T - t_L) \\ t_{\tau\tau} &= \frac{1}{4}(3t_L - t_T) \\ t_{n\tau} &= \frac{\sqrt{3}}{4}(t_T + t_L). \end{aligned} \tag{35}$$

In order to find the explicit spin-orbit coupling terms of Hamiltoinan (34), it is convenient to change to the circular polarization basis ($|+\rangle, |-\rangle$) instead of radial-azimuthal ($|n\rangle, |\tau\rangle$) via the transformation:

$$\begin{aligned} |j, n\rangle &= \frac{1}{\sqrt{2}} \left[\exp(-i2\pi \frac{j-1}{6}) |j, +\rangle + \exp(i2\pi \frac{j-1}{6}) |j, -\rangle \right] \\ |j, \tau\rangle &= \frac{1}{\sqrt{2}} \left[\exp(-i2\pi (\frac{j-1}{6} + \frac{1}{4})) |j, +\rangle + \exp(i2\pi (\frac{j-1}{6} + \frac{1}{4})) |j, -\rangle \right]. \end{aligned} \tag{36}$$

Next, for the spatial component of the wavefunction, we change to the basis of orbital angular momentum $|l\rangle$ ($l = 0, \pm 1, \pm 2, 3$) via the transformation

$$|l,\pm\rangle = \sum_{j=1}^{6} \exp(i\frac{l(j-1)2\pi}{6})\,|j,\pm\rangle\,. \tag{37}$$

In the orbital-circular polarisation basis, the Hamiltonian takes the form:

$$\begin{pmatrix}
E-2\hbar t & 0 & 0 & 0 & 0 & 0 & 0 & -\Delta E-\frac{\hbar\Delta t}{2} & 0 & 0 & 0 & 0 \\
0 & E-2\hbar t & 0 & 0 & 0 & 0 & 0 & 0 & -\Delta E-\frac{\hbar\Delta t}{2} & 0 & 0 & 0 \\
0 & 0 & E-\hbar t & 0 & 0 & 0 & 0 & 0 & 0 & 0 & 0 & -\Delta E+\frac{\hbar\Delta t}{2} \\
0 & 0 & 0 & E-\hbar t & -\Delta E-\hbar\Delta t & 0 & 0 & 0 & 0 & 0 & 0 & 0 \\
0 & 0 & 0 & -\Delta E-\hbar\Delta t & E-\hbar t & 0 & 0 & 0 & 0 & 0 & 0 & 0 \\
0 & 0 & 0 & 0 & 0 & E-\hbar t & 0 & 0 & 0 & 0 & -\Delta E+\frac{\hbar\Delta t}{2} & 0 \\
0 & 0 & 0 & 0 & 0 & 0 & E+\hbar t & 0 & 0 & -\Delta E+\hbar\Delta t & 0 & 0 \\
-\Delta E-\frac{\hbar\Delta t}{2} & 0 & 0 & 0 & 0 & 0 & 0 & E+\hbar t & 0 & 0 & 0 & 0 \\
0 & -\Delta E-\frac{\hbar\Delta t}{2} & 0 & 0 & 0 & 0 & 0 & 0 & E+\hbar t & 0 & 0 & 0 \\
0 & 0 & 0 & 0 & 0 & 0 & -\Delta E+\hbar\Delta t & 0 & 0 & E+\hbar t & 0 & 0 \\
0 & 0 & 0 & 0 & 0 & -\Delta E+\frac{\hbar\Delta t}{2} & 0 & 0 & 0 & 0 & E+2\hbar t & 0 \\
0 & 0 & -\Delta E+\frac{\hbar\Delta t}{2} & 0 & 0 & 0 & 0 & 0 & 0 & 0 & 0 & E+2\hbar t
\end{pmatrix}
\begin{matrix} 0^+ \\ 0^- \\ +1^+ \\ +1^- \\ -1^+ \\ -1^- \\ +2^+ \\ +2^- \\ -2^+ \\ -2^- \\ 3^+ \\ 3^- \end{matrix}, \tag{38}$$

where

$$\begin{aligned} E &= \frac{1}{2}(E_\tau + E_n) \\ \Delta E &= \frac{1}{2}(E_n - E_\tau) \\ t &= \frac{1}{2}(t_L + t_T) \end{aligned} \tag{39}$$

This matricial form of the Hamiltonian is equivalent to Hamiltonian (29), showing the coupling between states of opposite orbital momentum and spin.

This Hamiltonian can also be expressed in operator form acting on a spinor $[\Psi_+(j)\Psi_-(j)]^T$, where j plays a role of generalized integer coordinate, $j = 1, ..., 6$. For this we introduce the diagonal part of the Hamiltonian $\hat{H}_0 = \hat{H}(\Delta E = \hbar\Delta t = 0)$. The eigenstates of $\hat{H}_0$ can be classified in terms of the orbital angular momentum l and produce the basis of Hamiltonian (38). Its eigenvalues E_l are

$$E_l = E - 2\hbar t \cos\left(\frac{2\pi l}{6}\right) \tag{40}$$

We can introduce an operator $\hat{M} = \frac{\partial^2 E_l}{\partial l^2} = \cos\left(\frac{2\pi l}{6}\right)$, which allows us to rewrite the Hamiltonian in the operator form:

$$\hat{H} = \hat{H}_0 - \Delta E \begin{pmatrix} 0 & e^{-2i\varphi_j} \\ e^{2i\varphi_j} & 0 \end{pmatrix} + \hbar\Delta t(\hat{M}\begin{pmatrix} 0 & e^{-2i\varphi_j} \\ e^{2i\varphi_j} & 0 \end{pmatrix} + \begin{pmatrix} 0 & e^{-2i\varphi_j} \\ e^{2i\varphi_j} & 0 \end{pmatrix}\hat{M}), \tag{41}$$

where $\varphi_j = j2\pi/6$.

It is also possible to represent the same Hamiltonian in a more compact form using an operator $\hat{K}$ which returns the cosine of the sum of orbital momentum and spin:

$$\left\langle l \left| \hat{K} \right| l \right\rangle = \cos(l + \sigma). \tag{42}$$

Then, Hamiltonian (38) can be expressed

$$\hat{H} = \hat{H}_0 - \Delta E \begin{pmatrix} 0 & e^{-2i\varphi_j} \\ e^{2i\varphi_j} & 0 \end{pmatrix} + \hbar\Delta t\hat{K}\begin{pmatrix} 0 & e^{-2i\varphi_j} \\ e^{2i\varphi_j} & 0 \end{pmatrix}. \tag{43}$$